Iron–Titanium Oxide Nanocomposites Functionalized with Gold Particles: From Design to Solar Hydrogen Production

Davide Barreca, Giorgio Carraro, Alberto Gasparotto, Chiara Maccato, Michael E. A. Warwick, Elisa Toniato, Valentina Gombac, Cinzia Sada, Stuart Turner, Gustaaf Van Tendeloo, and Paolo Fornasiero**

***Hematite*–titania nanocomposites, eventually functionalized with gold nanoparticles (NPs), are designed and developed by a plasma-assisted strategy, consisting in: (i) the plasma enhanced-chemical vapor deposition of α-Fe_2O_3 on fluorine-doped tin oxide substrates; the radio frequency-sputtering of (ii) TiO_2, and (iii) Au in controlled amounts. A detailed chemicophysical characterization, carried out through a multitechnique approach, reveals that the target materials are composed by interwoven α-Fe_2O_3 dendritic structures, possessing a high porosity and active area. TiO_2 introduction results in the formation of an ultrathin titania layer uniformly covering Fe_2O_3, whereas Au sputtering yields a homogeneous dispersion of low-sized gold NPs. Due to the intimate and tailored interaction between the single constituents and their optical properties, the resulting composite materials are successfully exploited for solar-driven applications. In particular, promising photocatalytic performances in H_2 production by reforming of water–ethanol solutions under simulated solar illumination are obtained. The related insights, presented and discussed in this work, can yield useful guidelines to boost the performances of nanostructured photocatalysts for energy-related applications.**

Dr. D. Barreca
CNR-ICMATE and INSTM
Department of Chemistry
Padova University
35131 Padova, Italy
Dr. G. Carraro, Dr. A. Gasparotto, Prof. C. Maccato, Dr. M. E. A. Warwick, Dr. E. Toniato
Department of Chemistry
Padova University and INSTM
35131 Padova, Italy
E-mail: chiara.maccato@unipd.it
Dr. V. Gombac, Prof. P. Fornasiero
Department of Chemical and Pharmaceutical Sciences
ICCOM-CNR Trieste Research Unit
INSTM Research Unit
Trieste University
34127 Trieste, Italy
E-mail: pfornasiero@units.it
Prof. C. Sada
Department of Physics and Astronomy
Padova University
35131 Padova, Italy
Dr. S. Turner, Prof. G. Van Tendeloo
EMAT
University of Antwerp
2020 Antwerpen, Belgium

DOI: 10.1002/admi.201600348

1. Introduction

With the depletion of fossil fuels and the environmental concerns related to their combustion,[1–3] the availability of renewable energy sources has become a crucial research focus.[4–10] Among the possible alternatives, sunlight-driven H_2 generation using semiconductor photocatalysis[6,11–28] is a clean approach for a viable utilization of solar energy,[23,29] in the production of a carbon-free energy carrier.[1,5,12,24,30–34] In this regard, TiO_2 is considered to be the most interesting candidate for commercial scale-up[35] thanks to its favorable photocatalytic properties, as well as low cost, nontoxicity, and chemical stability.[5,27,34,36–38] Nevertheless, detrimental issues such as the fast charge carrier recombination in titania[39,40] and its large band gap (E_G = 3.2 eV),[17,26,41,42] resulting in the sole absorption of UV photons[11,28,35] (≈4% of the whole solar spectrum),[7] severely limit TiO_2 applications in sunlight and indoor environment.[1,36,43,44] To extend TiO_2 photoactivity into the visible (vis) region and minimize recombination phenomena, several approaches have been undertaken, including doping with metals/nonmetals[2,32,34,41] and preparation of TiO_2-based composites involving other active materials.[38,40,45,46] In this regard, another promising photocatalyst is *hematite* (α-Fe_2O_3),[16,18,23,29,47] an *n*-type semiconductor with a smaller band gap (E_G = 2.2 eV),[22,48] enabling vis light absorption.[1,5,8,11,14,44] Similarly to TiO_2, Fe_2O_3 is environmentally friendly, inexpensive and stable.[6,46,49,50] Nevertheless, its main disadvantages are the low carrier mobility,[45,48] the limited excited state lifetime[11] and the short hole diffusion length (<4 nm),[3,6,20,22,29] confining the effective photon absorption within ≈10 nm of the surface[5,19,21] and leading to a lower H_2 photoproduction efficiency.[1,14,19,36]

As a matter of fact, the tailored fabrication of Fe_2O_3–TiO_2 nanocomposites is a valuable mean to synergistically exploit the single oxide advantages,[43,45] yielding improved properties both in direct photocatalysis[3,11,36,41–43,49] and in photoelectrochemical (PEC) H_2O splitting.[6,10,51] Specifically, it has been reported that Fe_2O_3 functionalization with an ultrathin TiO_2 surface layer, beside passivating Fe_2O_3 surface trap states, allows the tailoring of light absorption and charge carrier transport phenomena through the precise engineering of the resulting

heterointerface. Nonetheless, an ad hoc surface layer can also offer an improved corrosion protection to the underlying iron oxide matrix, an important issue in view of practical applications.[6,10,45,52–54] It is worth highlighting that, in spite Fe_2O_3 modification with an ultra-thin TiO_2 overlayer has been demonstrated to promote a remarkable structural and electronic interplay at the Fe_2O_3/TiO_2 interface, only very few studies on this topic have been published to date.[6,10,54]

To further enhance Fe_2O_3-TiO_2 functional performances, a viable route has been proven to be the functionalization with noble metal (especially Au) particles. In particular, the formation of metal-oxide Schottky junctions[19,26,37,40] has a key role in minimizing the recombination of photogenerated charge carriers.[21,55] To date, various works have been devoted to the influence of gold NPs on the photoactivity of Fe_2O_3[19–22] and TiO_2[24–27,32,40] for hydrogen production. In regard to composite Fe_2O_3–TiO_2 systems, previous works have been dedicated to their functionalization with metal Ag/Au NPs only for PEC water splitting.[1,5] In a different way, reports on H_2 production by direct photocatalysis have been focused only on gold-free Fe_2O_3–TiO_2 powdered composites.[2,3,31,36,43] So far, no studies on supported nanosystems, enabling to avoid filtration processes and minimize undesired aggregation phenomena,[42,46,56] are available. The catalytic applications of Fe_2O_3–TiO_2–Au materials have encompassed CO, industrial wastewater oxidation[9,57–59] and H_2 production from methanol,[30] but, to our knowledge, their use in H_2 photogeneration by direct photocatalysis has never been reported.

Herein, we demonstrate the use of Fe_2O_3–TiO_2–Au nanosystems to boost the H_2 yield under solar illumination, a largely available and intrinsically renewable natural energy source, in the absence of any external electrical bias. The advantages brought about by the present nanomaterials encompass an enhanced photon absorption,[1,5] along with a suppressed exciton recombination due to the interfacial charge transfer at the Fe_2O_3–TiO_2–Au interfaces.[1,5,28,34,55,60] In this work, Fe_2O_3–TiO_2–Au nanosystems were fabricated by an original multistep plasma-assisted approach, allowing a fine tailoring of the system morphology and of the resulting functional performances.[39,43] In particular, Fe_2O_3 nanostructures were initially grown by plasma enhanced-chemical vapor deposition (PE-CVD) on fluorine-doped tin oxide (FTO) substrates and subsequently subjected to the sequential radio frequency (RF)-sputtering of TiO_2 and Au at low temperatures, in order to avoid detrimental alterations of the pristine oxide systems. Efforts have been devoted to exploiting the synergy between the typical infiltration power characterizing RF-sputtering and the porosity of the initial oxide matrices[4,13] to achieve a controlled dispersion of gold nanoparticles and an intimate contact with the oxide system. Complementary experimental observations have been adopted to investigate the underlying nucleation and growth mechanisms, with particular attention to the interfacial relationships occurring between the various constituents. Finally, the functional behavior of the obtained systems was investigated in H_2 production by photoreforming of renewable sources (i.e., bioethanol aqueous solutions).[25] The benefits offered by photoreforming over direct water splitting have already been reported in relation to various metal oxide systems.[4,7,12,46,56] In this work, the performances of the target nanomaterials are presented and discussed for the first time, evidencing how a careful control of the composite assembly is the key factor to beneficially affect the system chemical reactivity.

2. Results and Discussion

In this study, the characteristics of the target materials were investigated as a function of their composition, introducing each constituent step by step (Fe_2O_3–TiO_2, Fe_2O_3–Au, Fe_2O_3–TiO_2–Au) with the aim of understanding the effects originating from variations in their electronic/chemical coupling. For comparison purposes, relevant properties of bare Fe_2O_3, as well as TiO_2-based samples (see the Supporting Information), were also analyzed. In order to perform a preliminary investigation of the system morphology and organization as a function of composition, field emission-scanning electron microscopy (FE-SEM) studies were undertaken and relevant results are presented in **Figure 1** for Fe_2O_3–Au and Fe_2O_3–TiO_2–Au samples. As a general rule, FE-SEM images evidenced the presence of high-density interwoven nanoflakes, resembling the ones occurring on bare Fe_2O_3 (Supporting Information, Figure S1), whose interconnection resulted in the formation of branched structures. After functionalization with Au (Figure 1a–c), the system morphology did not undergo major modifications with respect to bare iron(III) oxide. A careful analysis of the recorded images enabled to discern that Fe_2O_3 aggregates were uniformly decorated by low-sized NPs, with average dimensions of (6 ± 2) nm. This value remained unaltered if gold sputtering was performed over Fe_2O_3–TiO_2 specimens, instead of bare Fe_2O_3 (compare Figures 1b and 1e). Such a result indicated that, under the adopted processing conditions, gold NP nucleation was not significantly affected by the nature of the underlying material. TiO_2 deposition on Fe_2O_3 nanostructures produced a more rounded surface morphology (Figure 1d vs 1a). Cross-sectional FE-SEM images (Figure 1c; compare also Supporting Information, Figure S1) revealed the occurrence of dentritic structures, with voids extending deep into the nanodeposits, resulting in porous systems. The presence of similar arrays has been reported to be beneficial for light trapping/scattering phenomena, ultimately favoring also an improved light harvesting.[14] On the other hand, the use of porous structures is advantageous in order to attain a higher contact area with the reaction medium.[50,56] Estimation of thickness values yielded a mean value of (300 ± 30) nm for Fe_2O_3–Au and Fe_2O_3–TiO_2–Au specimens, respectively, revealing no net increase upon functionalization with titania and gold in comparison with bare Fe_2O_3 (Supporting Information, Figure S1). In line with this observation, atomic force microscopy (AFM) analyses (Supporting Information, Figure S2) did not reveal significant morphological differences for the target nanomaterials. All the specimens were characterized by a granular-like topography, with an average root-mean-square (RMS) roughness value of ≈28 nm, independent on the synthesis conditions. The system structure was preliminarily analyzed by means of X-ray diffraction (XRD, Supporting Information, Figure S3). The obtained patterns revealed the presence of reflections pertaining to rhombohedral α-Fe_2O_3

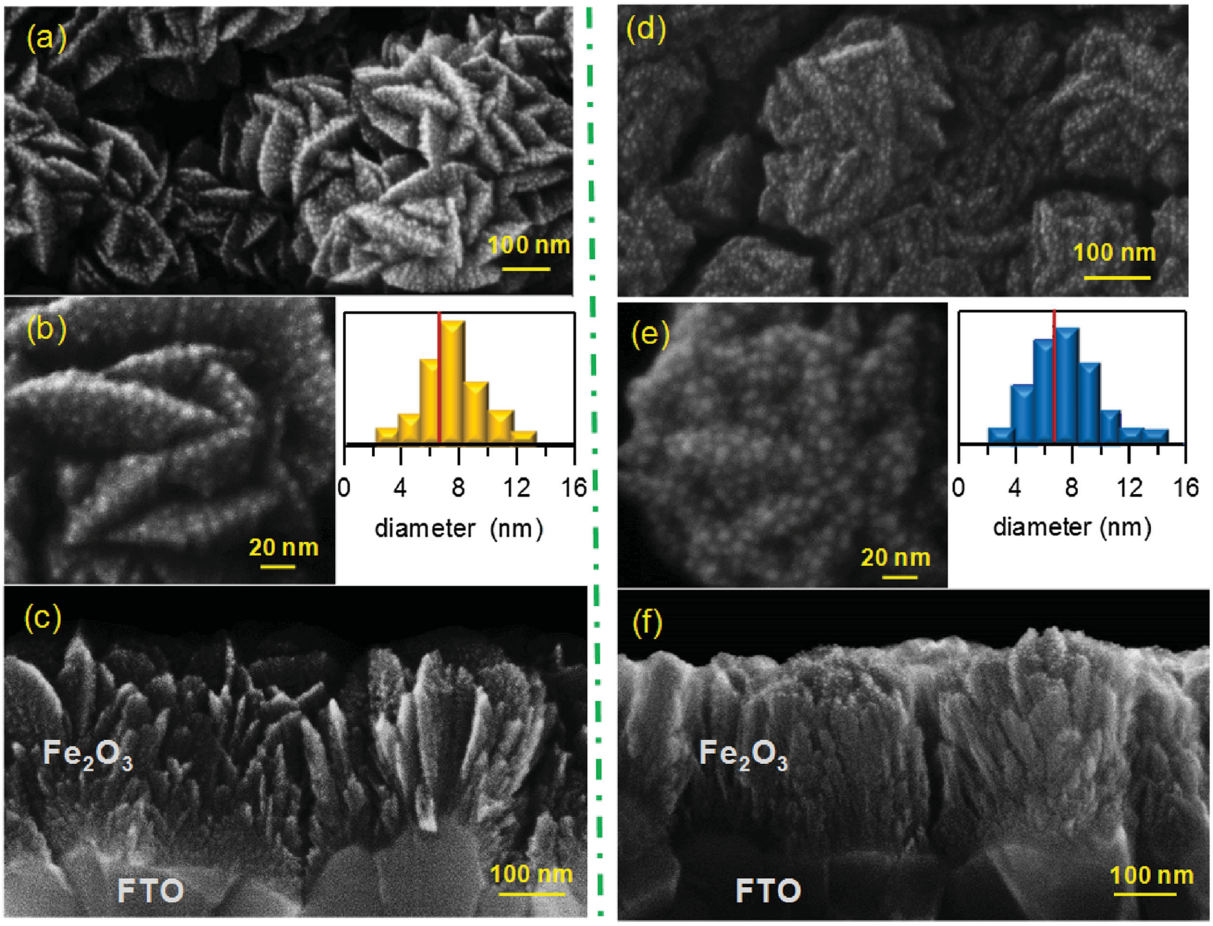

Figure 1. Representative plane-view and cross-sectional FE-SEM images for a–c) Fe_2O_3–Au and d–f) Fe_2O_3–TiO_2–Au specimens. In each case, the histogram of Au particle size distribution is also reported.

(*hematite*)[61] as the sole iron(III) oxide polymorph. The relatively low peak intensity indicated a modest system crystallinity, which, in turn, could be traced back to the low adopted deposition temperature (see the Experimental Section). No other signals related to TiO_2 polymorphs and/or Au could be clearly observed, likely due to the low titania amount[10] and high Au NPs dispersion,[13,51] as confirmed by transmission electron microscopy (TEM) results. As a matter of fact, the latter analyses enabled to attain a deeper insight into the system nanostructure, with particular regard to TiO_2 and Au spatial distribution. To this regard, **Figure 2**a displays a high angle annular dark field-scanning TEM (HAADF-STEM; *Z* contrast) overview image for a Fe_2O_3–TiO_2–Au specimen. The energy dispersive X-ray spectroscopy (EDXS) elemental maps for Si, Sn, Fe, Ti, and Au pertaining to the same region, proposed in Figure 2b, reveals that titania and gold are mostly concentrated in the outermost material region.

Higher magnification HAADF-STEM imaging provided important information on the Fe_2O_3/TiO_2/Au interfaces. In fact, Figure 2c evidenced that the Fe_2O_3 nanoflakes were uniformly covered by rounded Au nanoparticles with a mean size in excellent agreement with FE-SEM results (compare Figure 1). Representative high resolution HAADF-STEM images displayed in Figure 2d revealed the presence of an amorphous titania deposit, whose very low thickness (close to 2 nm) prevented its clear observation by FE-SEM measurements.[10] The obtainment of amorphous TiO_2 could be of interest in view of possible applications of the target materials in photoelectrochemical water splitting, in order to boost photoanode performances in H_2O photooxidation.[62] In addition, high resolution HAADF-STEM images evidenced the polycrystalline nature of Au nanoparticles. Data displayed in Figure 2e–g, with particular regard to the EDXS elemental maps, clearly confirmed the presence of both TiO_2 and Au in the outermost sample region. Interestingly, a more detailed inspection revealed also an in-depth penetration of both TiO_2 and Au, as evidenced by the tailing of the corresponding signals in Figure 2f–g and confirmed by secondary ion mass spectrometry (SIMS) analyses (see below). This intimate contact between the composite constituents favorably affected the Fe_2O_3–TiO_2–Au reactivity in H_2 photoproduction (see below). Taken together, FE-SEM and TEM data demonstrated that the outer material region comprised all the three Fe_2O_3, TiO_2, and Au components. As regards Fe_2O_3–Au, an overview of representative HAADF-STEM and EDXS data is presented in the Supporting Information, Figure S4. As can be noticed, apart from the absence of titania, the observed features were similar to those illustrated in relation to Figure 2. The Fe_2O_3 near-surface region was decorated by evenly distributed

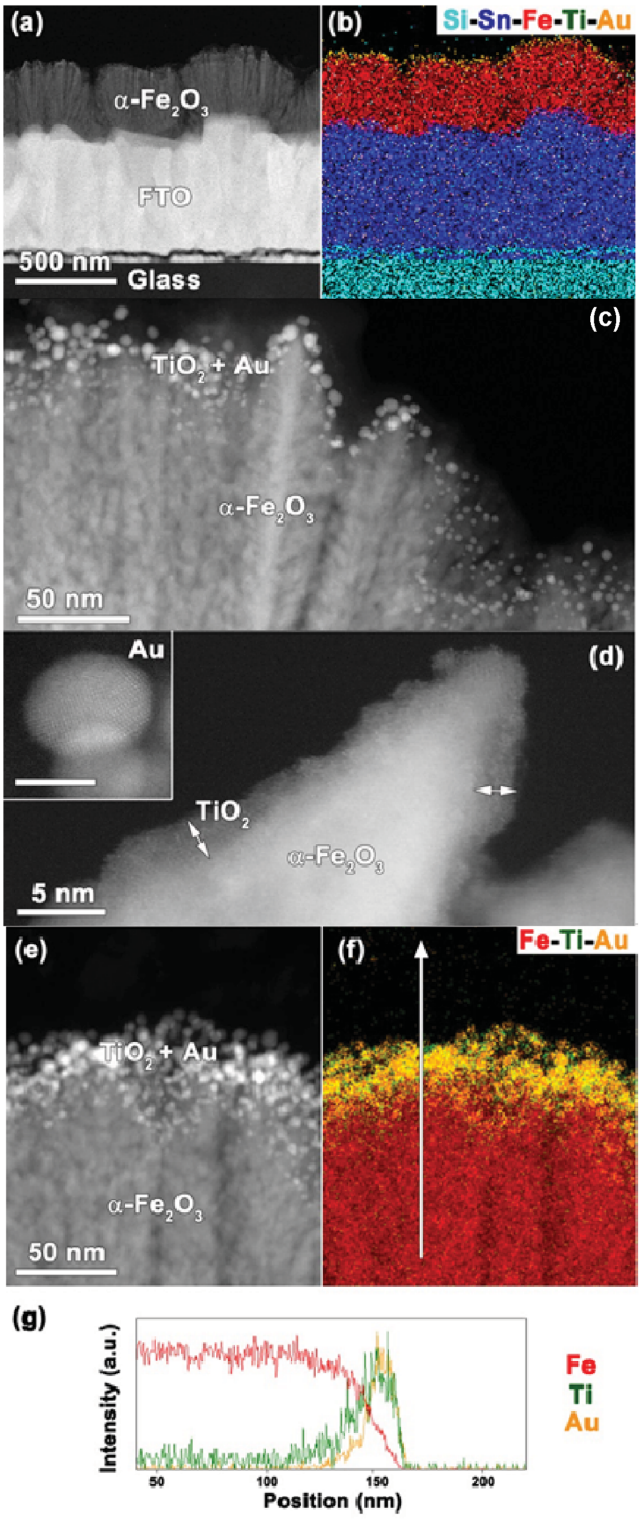

Figure 2. a) Cross-sectional HAADF-STEM overview image of a Fe_2O_3–TiO_2–Au specimen. b) Corresponding EDXS chemical map. c) HAADF-STEM image of the Fe_2O_3/TiO_2/Au interface. d) HAADF-STEM image of the Fe_2O_3/TiO_2 interface. The inset shows a high resolution HAADF-STEM image of polycrystalline Au nanoparticles. e) HAADF-STEM and f) EDXS elemental map of the Fe_2O_3/TiO_2/Au interface. The intensity profile along the arrow in (f), plotted in (g), clearly shows the presence of Ti and Au in the outermost Fe_2O_3 region.

Au nanoparticles with a rounded shape and an average size of (6 ± 2) nm, in excellent agreement with FE-SEM data.

The surface and in-depth composition was analyzed by the combined use of X-ray photoelectron spectroscopy (XPS) and SIMS. For sample Fe_2O_3–TiO_2–Au, wide scan XPS spectra (Supporting Information, Figure S5a) evidenced the presence of Au, Ti, Fe, and O, along with C signals arising from adventitious contamination. For all specimens, the position of the Fe2p spin-orbit components [binding energy (BE) ($Fe2p_{3/2}$) = 711.1 eV; BE ($Fe2p_{1/2}$) = 724.8 eV], along with the very weak *shake-up* satellites located at BE ≈9 eV higher than the main spin-orbit split components, are characteristic of Fe(III) centers in Fe_2O_3,[8,10,14] free from other oxidation states in appreciable amounts.[43,44,51,58,63] Irrespective of the adopted processing conditions, the presence of iron was always detected on the sample surface. This observation suggested a certain dispersion of both TiO_2 and Au into the Fe_2O_3 deposit, as indeed confirmed by EDXS and SIMS data analysis, and was in line with the very low TiO_2 thickness discussed in relation to Figure 2d (see also above).

The absence of any net Fe2p BE shift upon going from bare iron(III) oxide (Supporting Information, Figure S5c) to TiO_2-containing samples (**Figure 3**a) enabled to rule out the formation of ternary phases in appreciable amounts,[2,43] in accordance with results provided by the other characterization techniques. In fact, the Ti2p peaks were unaltered with respect to a bare TiO_2 specimen (Figure 3b), and could be fitted with a single doublet [BE($Ti2p_{3/2}$) = 458.9 eV; spin-orbit splitting = 5.7 eV], whose features were in line with the occurrence of Ti(IV) in TiO_2 (see also Supporting Information, Figure S5b).[9,10,34,45,58] The mean titanium content was ≈24 and ≈12 at% at the system surface for Fe_2O_3–TiO_2 and Fe_2O_3–TiO_2–Au samples, respectively. The $Au4f_{7/2}$ peak position (BE = 84.1 eV; spin-orbit splitting = 3.7 eV; Figure 3c) indicated the presence of metallic Au particles,[21,24–26,30,59,63] with no appreciable BE variation with respect to bulk Au.[27,32,40] For both the Fe_2O_3–Au and Fe_2O_3–TiO_2–Au samples, the mean gold surface content was evaluated to be ≈66 at%, in line with a very similar Au NPs dispersion and average size in both samples (see above).

Finally, two components contributing to the surface O1s photopeak were present (Figure 3d). The main band (I), centered at BE = 530.0 eV, was attributed to lattice oxygen in Fe and Ti oxides,[3,13,21,44] whereas component (II) at BE = 531.8 eV (typically ≈20% of the total O signal) was ascribed to the concurrence of adsorbed oxygen/surface –OH groups arising from contact with the outer atmosphere.[3,34,42,51] Relevant information on in-depth chemical composition, with particular regard to the mutual distribution of the various species, was gained by SIMS. Figure 3e,f compares the profiles pertaining to Fe_2O_3–TiO_2 and Fe_2O_3–TiO_2–Au specimens. In general, the carbon content was lower than 100 ppm, evidencing the purity of the synthesized materials. In all cases, a homogeneous distribution of Fe and O ionic yields throughout the nanodeposit thickness could be observed, confirming the uniform formation of iron(III) oxide. As can be noticed, the outermost sample region was Ti-rich, in line with the above observations (see Figure 2 and related comments). At higher depth values, titanium signals underwent a slow decrease up to a stable level, before dropping off at the interface with the substrate. This phenomenon suggested a notable intermixing between iron

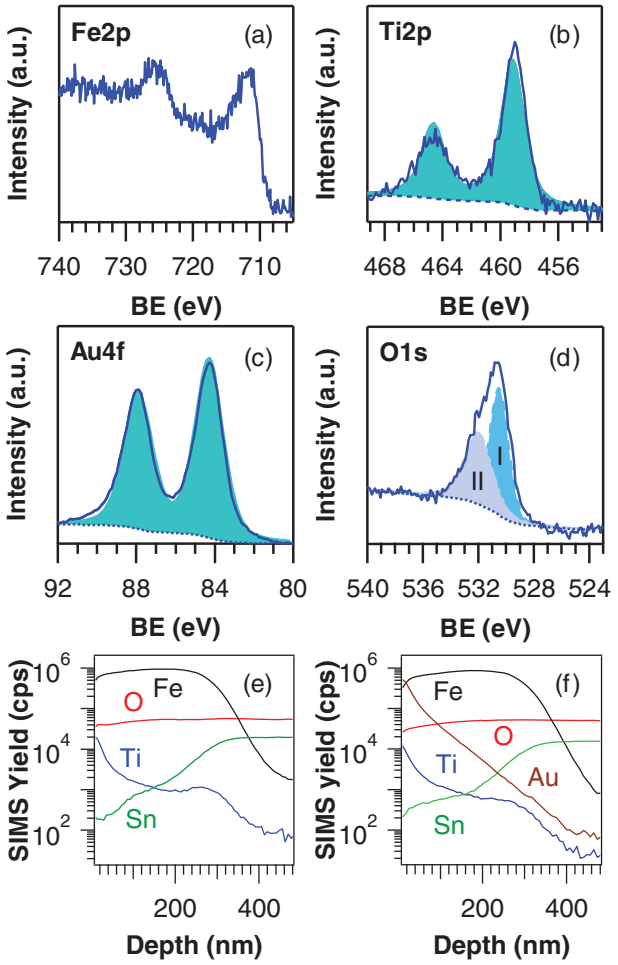

Figure 3. Surface and in-depth compositional analyses. a) Fe2p, b) Ti2p, c) Au4f, and d) O1s surface XPS peaks for a representative Fe_2O_3–TiO_2–Au sample. SIMS depth profiles for e) Fe_2O_3–TiO_2 and f) Fe_2O_3–TiO_2–Au specimens.

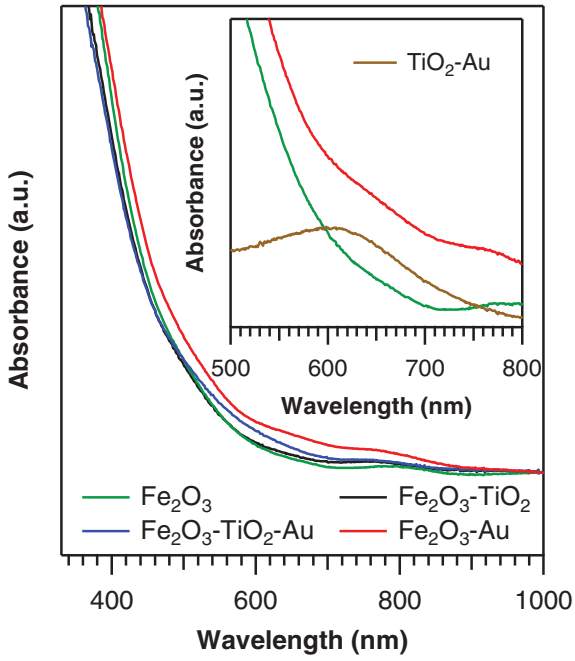

Figure 4. Optical absorption spectra of the investigated nanomaterials. Inset: Au SPR region for Fe_2O_3, Fe_2O_3–Au, and TiO_2–Au samples.

and titanium oxides, as previously mentioned. Upon gold functionalization (Figure 3f), no significant variation of Fe, Ti, and O profiles took place. It is worthwhile observing that the Au ionic yield displayed an erfchian profile,[13] with a progressively decreasing intensity at higher depth. Since the presence of SIMS artifacts could be excluded due to the adopted high mass resolution (HMR) configuration, these results confirmed that the adopted synthetic strategy enabled an efficient and homogeneous in-depth dispersion of both TiO_2 and Au NPs in Fe_2O_3. The observed behavior could be attributed to the synergy between the inherent porosity of the iron(III) oxide deposits and the high infiltration power of the sputtering technique,[13,64] further enhanced by plasma bombardment. In fact, due to the low processing temperatures (≤100 °C) and the absence of any ex situ annealing (see the Experimental Section), significant thermal effects could be discarded. For the same reasons, the Sn tailing extending into the nanodeposits could not be attributed to tin diffusion from the FTO substrate, at variance with previous studies,[13,14,51] but rather traced back to the inherently high roughness of the used FTO substrates, evidenced by images displayed in Figure 1c,f.

Taken together, the above observations demonstrate the formation of Fe_2O_3–TiO_2–Au nanocomposites with an intimate contact between all the constituents. This feature is extremely promising in view of hydrogen photogeneration, thanks to the possibility of exploiting the mutual interactions between the various composite components.

Optical properties of the materials in the UV–vis-NIR range were investigated using absorption spectroscopy. The recorded profiles, displayed in **Figure 4**, are very similar to those reported for pure iron(III) oxide nanomaterials,[14] in accordance with the fact that Fe_2O_3 is the main component of the target systems. Whereas the introduction of TiO_2 did not induce any major change with respect to the case of bare Fe_2O_3, a slight absorbance increase could be noticed upon Au introduction. This phenomenon can be better appreciated from the inset in Figure 4, showing an enlargement of the 500–800 nm wavelength range, in which the gold surface plasmon resonance (SPR) peak should be located.[1,26,27,32,34,37] In particular, this band can be appreciated at $\lambda \approx 600$ nm for the TiO_2–Au specimen.[24,27,40] A detailed spectra comparison highlighted the presence of a modest SPR contribution for the Fe_2O_3–Au specimen[19,21,22] (inset in Figure 4).

The optical band gaps for Fe_2O_3 and Fe_2O_3–TiO_2 samples were determined from Tauc plots (Supporting Information, Figure S6), assuming the occurrence of direct allowed electronic transitions.[14,45,47] The obtained values (E_G = 2.20 ± 0.05 eV) were in good agreement with those for Fe_2O_3[45] and Fe_2O_3–TiO_2 specimens,[51] and suggested that TiO_2 introduction did not appreciably affect the system optical properties in the vis interval.[51]

Hydrogen photoproduction was achieved under simulated solar light without the application of any external bias. Preliminary control experiments demonstrated that no H_2 generation

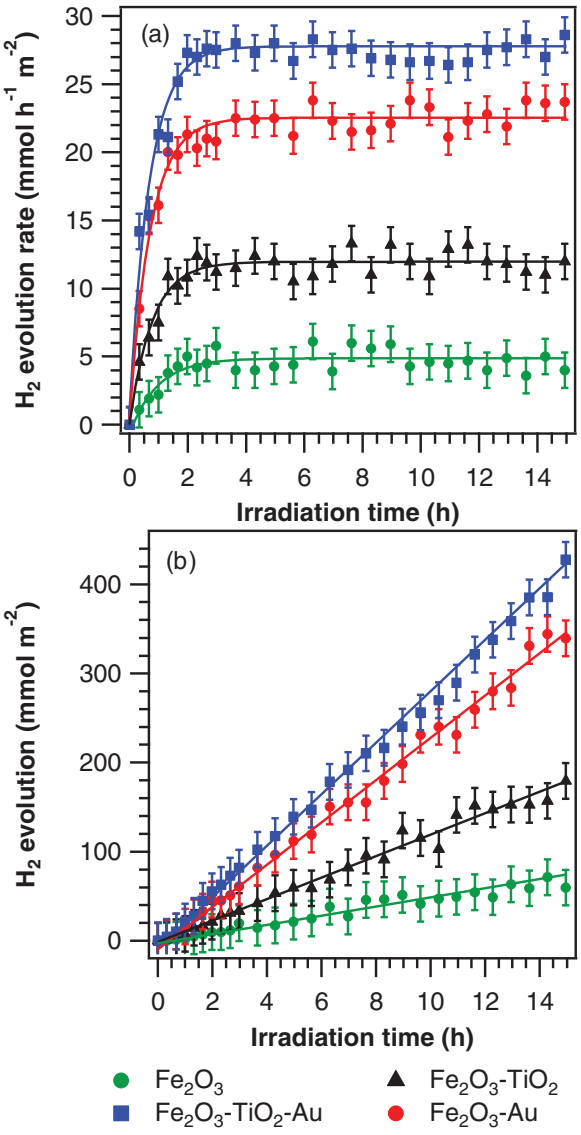

Figure 5. a) H_2 evolution rates and b) integrated H_2 production obtained during the photoreforming of water–ethanol solutions under simulated solar illumination.

took place without illumination or in the absence of the target materials. The results obtained for the different samples are presented in **Figure 5** as a function of the irradiation time. Even bare Fe_2O_3 and TiO_2 (see also Supporting Information, Figure S7) were able to drive H_2 production, though in small amounts. In fact, at variance with bulk Fe_2O_3, supported iron(III) oxide nanosystems possess the correct conduction band edge positions to promote proton reduction.[65] Therefore, the photocatalytic performances of bare Fe_2O_3 strongly depend on the specific preparation conditions and the resulting nano-organization.[12,50] Regardless of the used processing conditions, all the specimens presented an initial induction period (≈2 h), characterized by a progressive increase of the hydrogen yield up to a constant rate value (Figure 5a). This phenomenon suggested the occurrence of a light-induced surface activation and the subsequent establishment of an equilibrium between by-products adsorbed on the catalyst surface and in the liquid/gas phase.[56] It is worthwhile observing that H_2 yields were almost constant for irradiation times >14 h, evidencing an appreciable stability upon prolonged utilization, and no significant photocorrosion phenomena. The linear trends observed in Figure 5b are in agreement with the long term time stability of the system photocatalytic performances, of great interest for possible practical applications.[43,46]

The mechanism by which H_2 is produced via photoreforming of H_2O/ethanol solutions proceeds by ethanol absorption on a surface adsorption site (∗), leading to ethoxide species (1). Subsequent reaction with a photogenerated hole (h^+) results in the production of acetaldehyde (2), quickly desorbed from the photocatalyst surface. Surface adsorbed hydrogen ions $H^+_{(ads)}$ can then lead to H_2 formation (3).[12,50] The overall process can be schematically described as follows:

$$CH_3CH_2OH + * \rightarrow CH_3CH_2O^-_{(ads)} + H^+_{(ads)} \quad (1)$$

$$CH_3CH_2O^-_{(ads)} + h^+ \rightarrow CH_3CHO_{(ads)} + H^+_{(ads)} + e^- \quad (2)$$

$$2H^+_{(ads)} + 2e^- \rightarrow H_{2(ads)} \rightarrow H_{2(g)} \quad (3)$$

Consistently with the proposed mechanism, acetaldehyde formation, parallel to the hydrogen evolution, was observed both in the liquid and in the gas phase. Products of subsequent oxidation, such as acetic acid or CO_2, were not detected, likely due to the volatility of the former product that, in the presence of an ethanol excess, is quickly displaced from the photocatalyst surface, preventing thus any further oxidation.

A detailed inspection of the obtained results (Figure 5) evidenced that H_2 evolution rates displayed an enhancement according to the following trend: Fe_2O_3 < Fe_2O_3–TiO_2 < Fe_2O_3–Au < Fe_2O_3–TiO_2–Au. Correspondingly, hydrogen yields normalized by the active catalyst mass (mmol h^{-1} g^{-1}) increased in the order 3.7 < 9.0 < 16.9 < 20.9. Interestingly, the Fe_2O_3–TiO_2–Au material displayed a hydrogen production rate more than five times higher than bare Fe_2O_3 systems. Notably, the corresponding value compared favorably with one of the state-of-the-art photocatalysts, black hydrogenated titania functionalized with Pt NPs,[66] and P25 TiO_2 functionalized with Au NPs.[33] The validity of the present results is further highlighted by the use of supported nanosystems with a minimal amount of active material, that enable to avoid sintering/filtration problems typically presented by powdered photocatalysts[42,46] and pave thus the way for real-world applications.

The above reported performance trend was evident also analyzing the solar-to-fuel efficiency (SFE) values obtained under simulated sunlight irradiation (defined as reported in the Supporting Information): Fe_2O_3 (0.02%) < Fe_2O_3–TiO_2 (0.05%) < Fe_2O_3–Au (0.09%) < Fe_2O_3–TiO_2–Au (0.11%). Despite the obtained values were not very high, the present data indicated a clear dependence of functional performances on the actual system composition and nanostructure, taking into account that, as already mentioned, bulk Fe_2O_3 is inactive in the target process.[65] It is worth noticing that, for the best performing specimen, the evaluated SFE was higher

than those previously reported for PE-CVD α-Fe_2O_3-based nanosystems.[50,67]

The very favorable performances of the present materials can be traced back to their unique morphological organization.[43] In fact, the presence of voids, extending deep into the system structure (see the above morphological data), exposes also the internal surface to the reaction medium, providing short carrier transport distances and suppressing undesired recombination processes.[47] Nevertheless, significant contributions from the system surface area to the above reported reactivity order can be excluded, since all the analyzed materials displayed similar surface roughness (see above), the latter parameter being, in turn, proportional to the active area.[14] To better understand the above reported reactivity order, it is worthwhile considering that Fe_2O_3–TiO_2 composites performed better than the single oxides (see also Supporting Information, Figure S7) thanks to the formation of Fe_2O_3–TiO_2 heterojunctions, which resulted in an improved charge carrier separation[11,39,41,42,49] that, in turn, had a direct beneficial effect to drive the target H_2 photogeneration. In addition, Figure 5 shows that Fe_2O_3–Au systems provided a systematically higher hydrogen yield than Fe_2O_3–TiO_2 ones. This phenomenon can be interpreted basing on the concurrence of two main effects. First, the formation of Schottky junctions between iron(III) oxide and Au NPs is favorable in suppressing detrimental recombination processes, making photogenerated electrons more easily available for hydrogen formation.[50] In addition, Au nanoparticles can act as an antenna that localizes the optical energy and transfers it to the oxide semiconductors within ≈10 nm of the metal.[17,19,26] As far as Fe_2O_3–TiO_2–Au system is concerned, the best performances obtained herein can be explained taking advantages of the concomitant beneficial effects described above.[42,50]

The use of a cut off filter at 420 nm, in combination with simulated solar light, showed that the hydrogen production under pure visible light irradiation is negligible or within the experimental error and similar for all the investigated materials, indicating that the promising activity under simulated sunlight was mainly due to the absorption of the UV fraction. Basing on the obtained results, a possible mechanism accounting for the system behavior has been devised and proposed in **Figure 6**. Under simulated solar light, which comprises both UV and vis irradiation, efficient UV photon absorption occurs with electrons promotion from VBs into the corresponding CBs for both Fe_2O_3 and TiO_2. Subsequently, photogenerated electrons can be successfully transferred to Au NPs, acting as electron sinks,[1,26,35,50] and play a direct role in the reduction of H^+ to H_2.[55] The holes generated in this process can likely access the outermost material surface, thanks to the very low TiO_2 thickness (≈2 nm, as estimated by cross-sectional TEM analyses; see above and Figure 2d). To corroborate this observation, it is worth recalling that the hole diffusion length in TiO_2-based systems is typically comprised between 10 and 100 nm,[68,69] and that the use of thicker titania layers has detrimental effects on the resulting functional performances. Thanks to the capability of Au to collect photogenerated electrons, that reduce the extent of the e^-/h^+ recombination processes, the longer lifetime of the photoproduced holes results in a more efficient ethanol photooxidation.

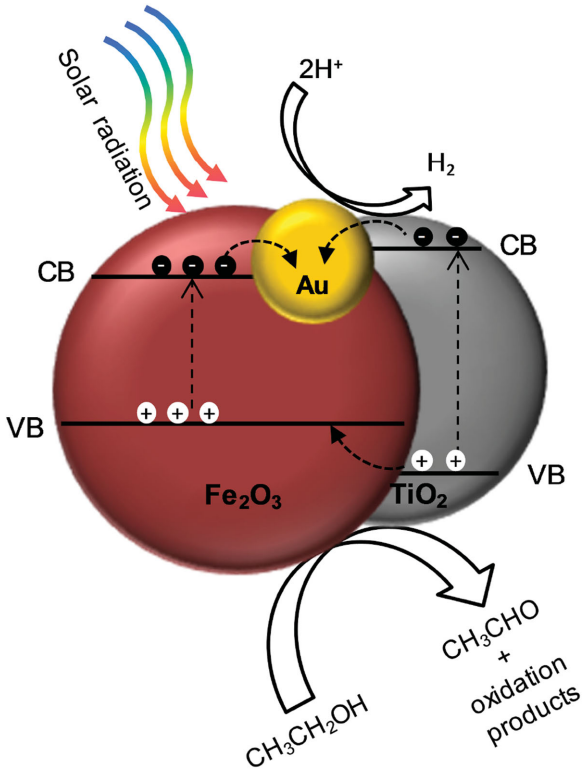

Figure 6. Simplified sketch of the main processes occurring during ethanol photoreforming under simulated solar illumination on Fe_2O_3–TiO_2–Au specimens (VB = valence band; CB = conduction band).

3. Conclusions

The present work has been focused on a low-temperature plasma-assisted route to the formation of multicomponent photocatalytic materials. The proposed strategy involved the PE-CVD of Fe_2O_3 nanomaterials on FTO substrates, resulting in porous systems that were subsequently functionalized with TiO_2 and Au NPs in tailored amounts. The adopted low-temperature synthetic protocol, which can be potentially extended to thermally labile substrates, enabled to avoid solid state reactions between Fe_2O_3 and TiO_2 and to fabricate pure and large-area nanocomposites. The latter were characterized by the formation of an amorphous titania layer uniformly covering the underlying α-Fe_2O_3 nanodeposits, and by an even dispersion of Au NPs characterized by a controllable spatial distribution. The intimate contact between the single components had a strategic importance to obtain highly promising H_2 production rates, achieved in the photoreforming of water–ethanol solutions promoted by solar illumination, without the need of any applied bias. The functional behavior of Fe_2O_3–TiO_2–Au photocatalysts was rationalized in terms of an enhanced carrier separation at the single component interface and an improved light harvesting, demonstrating the importance of morphological and compositional control in the development and mastering of advanced nanocomposites. To our knowledge, this work represents the first example of photoassisted H_2 production by supported Fe_2O_3–TiO_2–Au nanosystems produced by low-temperature plasma-assisted approaches.

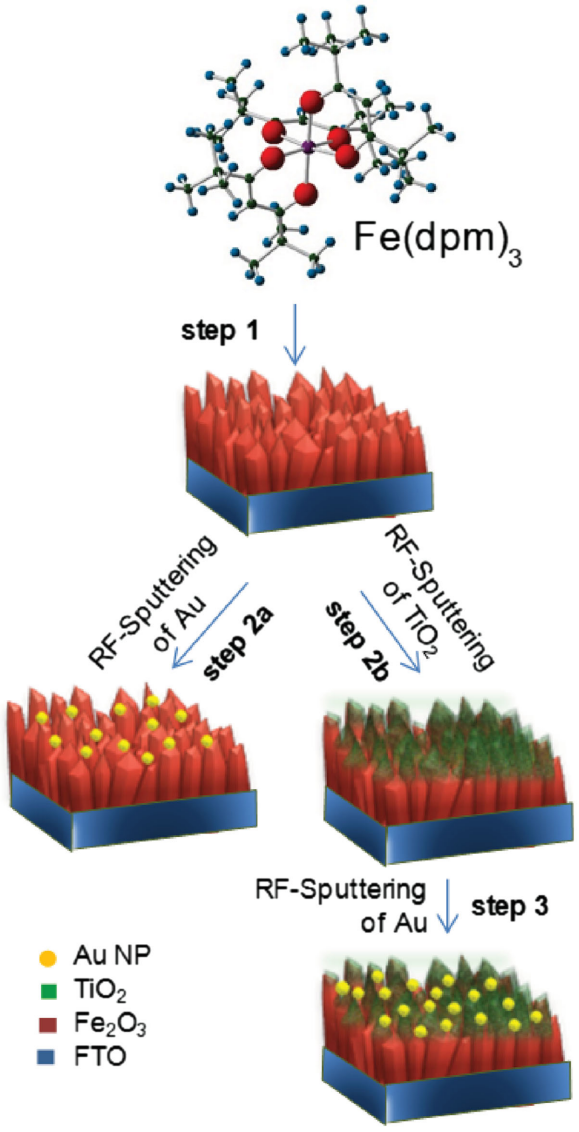

Scheme 1. Graphical representation of the synthetic approach adopted for the fabrication of the target oxide nanomaterials and their functionalization with Au NPs.

Basing on the present data, further efforts to improve the overall material performances will involve the concomitant optimization of Fe_2O_3 morphology, to obtain nanosystems endowed with higher porosity, and the possible use of higher TiO_2 and/or Au loadings to further enhance the system functional performances. In addition, the results presented herein pave the way for sustainable energy generation from abundant and renewable natural sources, as well as for technological applications even in other solar-driven processes, such as self-cleaning surfaces or wastewater purification. Our attention will be also devoted to the use of the target nanomaterials as photoanodes for PEC H_2O splitting applications, with particular regard to the interplay between their chemicophysical and functional properties as a function of ex situ thermal treatments in air. Research activities in this direction are already under way.

4. Experimental Section

Synthesis: The fabrication of the target materials was carried out by means of a stepwise vapor phase process, as illustrated in **Scheme 1**. Iron(III) oxide was deposited on FTO-coated glass substrates (Aldrich, 735167-1EA, lateral dimensions = 2.0 cm × 1.0 cm; FTO thickness = 600 nm) (Scheme 1, step 1), precleaned according to a well-established procedure.[64] Basing on previous experiments,[70] depositions were carried out at a substrate temperature of 100 °C using the following conditions: RF-power = 10 W; total pressure = 1.0 mbar; duration = 1 h. As concerns both titania layer thickness and Au loading, the data collected in the present work are the result of a series of optimization experiments carried out in our laboratories.[71] In particular, TiO_2 RF-sputtering on Fe_2O_3 deposits (Scheme 1, step 2b) was carried out under the following conditions: substrate temperature = 60 °C; Ar flow rate = 10 sccm; total pressure = 0.3 mbar; RF-power = 20 W; sputtering time = 3 h. After an initial prescreening of the operating conditions, the use of higher RF-powers or longer deposition times was intentionally avoided in order to prevent the obtainment of too compact systems with reduced active area, a feature detrimentally affecting the ultimate functional behavior in photo-assisted hydrogen production. Indeed, preliminary experiments involving longer titania deposition times (up to 5 h) yielded negligible H_2 photoproduction rates with respect to the present Fe_2O_3-TiO_2 materials. As a consequence, these conditions were discarded and the attention was focused on a process duration of 3 h for titania deposition.

Finally, basing also on previously reported results,[46] Au NPs were deposited on the obtained systems (Scheme 1, steps 2a/3) using the same conditions adopted for TiO_2 sputtering, apart from the RF-power (5 W) and the sputtering time (20 min). These parameters enabled to avoid the complete coverage of the underlying systems by a continuous gold overlayer. Further experimental details are reported in the Supporting Information.

Characterization: The average deposit mass, measured by using a Mettler Toledo XS105DU Microbalance, was evaluated to be 0.20 ± 0.02 mg.

FE-SEM images were collected by a Zeiss SUPRA 40 VP instrument, operating at a primary beam acceleration voltage of 10.0 kV, using an in-lens detector. The ImageJ (http://imagej.nih.gov/ij/, accessed: November 2015) picture analyzer software was used to estimate the average nanoparticle dimensions and thickness values by averaging over 100 independent measurements. AFM analyses were carried out by an NT-MDT SPM solver P47H-PRO apparatus operating in semicontact mode. After a plane fitting procedure, RMS roughness[42] values were obtained from 3 × 3 μm^2 images.

XRD analyses were run in reflection mode on a Dymax-RAPID X-ray microdiffractometer equipped with a cylindrical imaging plate detector, using CuKα radiation (λ = 1.54056 Å) and a collimator diameter of 300 µm. Conventional XRD patterns were obtained by integration of 2D images.

Cross-sectional samples for TEM investigation were prepared by ion milling in a Leica RES 102 ion mill. HAADF-STEM imaging and EDXS mapping experiments were carried out on a FEI Tecnai Osiris microscope, operated at 200 kV and equipped with a Super-X high solid angle EDXS detector. High resolution HAADF-STEM imaging was performed on a FEI Titan "cubed" microscope (acceleration voltage = 300 kV), using a convergence semiangle α of 22 mrad and a collection inner semiangle β of 50 mrad.

XPS analyses were conducted on a Perkin-Elmer Φ 5600ci instrument using a standard AlKα radiation (hν = 1486.6 eV), at working pressures <10^{-8} mbar. The obtained BE values (uncertainty = ±0.2 eV) were corrected for charging effects by assigning to the adventitious C1s signal a position of 284.8 eV.[63,72] After a Shirley-type background subtraction, O1s, Ti2p and Au4f raw spectra were fitted by means of a nonlinear least-squares deconvolution program (XPS Peak 4.1, http://xpspeak.software.informer.com/4.1/, accessed: July 2015), using Gaussian–Lorentzian peak shapes. The fitting results are displayed along with the raw spectra in Figure 3 and Figure S5 of the Supporting Information. Atomic percentages (at%) were calculated by photopeak integration, using standard PHI V5.4A sensitivity factors.

SIMS analyses were carried out by means of a IMS 4f mass spectrometer (Cameca) using a 14.5 keV Cs^+ primary beam (current = 30 nA, stability = 0.3%) and negative secondary ion detection. An electron gun was used for charge compensation. Beam blanking mode and HMR configuration were adopted to improve the in-depth resolution and avoid mass interference artifacts, respectively. Signals were recorded rastering over a 150×150 μm^2 area, sampling secondary ions from a sub-region close to 8×8 μm^2 in order to avoid crater effects. The erosion rate was evaluated by taking the depth of the erosion crater at the end of each analysis by a Tencor Alpha Step profilometer.

Optical absorption spectra were acquired operating in transmission mode and at normal incidence by means of a Cary 50 spectrophotometer, using bare FTO-coated glass substrate as a reference. In all cases, the substrate contribution was subtracted.

Photoreforming experiments were carried out from H_2O/CH_3CH_2OH mixtures under an Ar flow, using a Solar Simulator and an Atmospheric Edge Filter (cut-off at λ = 300 nm). On-line detection of hydrogen and volatile by-products was carried out by gas chromatography using Ar as carrier. Further technical details are reported in the Supporting Information.

Supporting Information

Supporting Information is available from the Wiley Online Library or from the author.

Acknowledgements

The authors kindly acknowledge the financial support under the FP7 project "SOLAROGENIX" (NMP4-SL-2012-310333), as well as Padova University ex-60% 2012–2015 projects, Grant No. CPDR132937/13 (SOLLEONE) and the post-doc fellowship ACTION, and Regione Lombardia-INSTM ATLANTE program. S.T. acknowledges the FWO Flanders for a post-doctoral scholarship. Many thanks are also due to Prof. E. Bontempi and Dr. M. Brisotto (Chemistry for Technologies Laboratory, Brescia University, Italy) for XRD analyses.

Received: April 26, 2016
Revised: June 16, 2016
Published online: July 20, 2016

[1] W. H. Hung, T. M. Chien, A. Y. Lo, C. M. Tseng, D. D. Li, *RSC Adv.* **2014**, *4*, 45710.
[2] M.-H. Pham, C.-T. Dinh, G.-T. Vuong, N.-D. Ta, T.-O. Do, *Phys. Chem. Chem. Phys.* **2014**, *16*, 5937.
[3] P. Luan, M. Xie, X. Fu, Y. Qu, X. Sun, L. Jing, *Phys. Chem. Chem. Phys.* **2015**, *17*, 5043.
[4] C. Maccato, D. Barreca, G. Carraro, A. Gasparotto, V. Gombac, P. Fornasiero, *Surf. Coat. Technol.* **2013**, *230*, 219.
[5] W.-H. Hung, T.-M. Chien, C.-M. Tseng, *J. Phys. Chem. C* **2014**, *118*, 12676.
[6] X. Yang, R. Liu, C. Du, P. Dai, Z. Zheng, D. Wang, *ACS Appl. Mater. Interfaces* **2014**, *6*, 12005.
[7] M. Cargnello, A. Gasparotto, V. Gombac, T. Montini, D. Barreca, P. Fornasiero, *Eur. J. Inorg. Chem.* **2011**, *2011*, 4309.
[8] A. A. Tahir, K. G. U. Wijayantha, S. Saremi-Yarahmadi, M. Mazhar, V. McKee, *Chem. Mater.* **2009**, *21*, 3763.
[9] A. Luengnaruemitchai, K. Srihamat, C. Pojanavaraphan, R. Wanchanthuek, *Int. J. Hydrogen Energy* **2015**, *40*, 13443.
[10] M. G. Ahmed, I. E. Kretschmer, T. A. Kandiel, A. Y. Ahmed, F. A. Rashwan, D. W. Bahnemann, *ACS Appl. Mater. Interfaces* **2015**, *7*, 24053.
[11] P. Luan, M. Xie, D. Liu, X. Fu, L. Jing, *Sci. Rep.* **2014**, *4*, 6180.
[12] G. Carraro, C. Maccato, A. Gasparotto, T. Montini, S. Turner, O. I. Lebedev, V. Gombac, G. Adami, G. Van Tendeloo, D. Barreca, P. Fornasiero, *Adv. Funct. Mater.* **2014**, *24*, 372.
[13] M. E. A. Warwick, D. Barreca, E. Bontempi, G. Carraro, A. Gasparotto, C. Maccato, K. Kaunisto, T.-P. Ruoko, H. Lemmetyinen, C. Sada, Y. Gönüllü, S. Mathur, *Phys. Chem. Chem. Phys.* **2015**, *17*, 12899.
[14] M. E. A. Warwick, K. Kaunisto, D. Barreca, G. Carraro, A. Gasparotto, C. Maccato, E. Bontempi, C. Sada, T.-P. Ruoko, S. Turner, G. Van Tendeloo, *ACS Appl. Mater. Interfaces* **2015**, *7*, 8667.
[15] C. X. Kronawitter, L. Vayssieres, S. Shen, L. Guo, D. A. Wheeler, J. Z. Zhang, B. R. Antoun, S. S. Mao, *Energy Environ. Sci.* **2011**, *4*, 3889.
[16] B. Iandolo, B. Wickman, I. Zoric, A. Hellman, *J. Mater. Chem. A* **2015**, *3*, 16896.
[17] S. C. Warren, E. Thimsen, *Energy Environ. Sci.* **2012**, *5*, 5133.
[18] S. K. Mohapatra, S. E. John, S. Banerjee, M. Misra, *Chem. Mater.* **2009**, *21*, 3048.
[19] E. Thimsen, F. Le Formal, M. Grätzel, S. C. Warren, *Nano Lett.* **2011**, *11*, 35.
[20] J. Wang, S. Pan, M. Chen, D. A. Dixon, *J. Phys. Chem. C* **2013**, *117*, 22060.
[21] L. Wang, X. Zhou, N. T. Nguyen, P. Schmuki, *ChemSusChem* **2015**, *8*, 618.
[22] P. S. Archana, N. Pachauri, Z. Shan, S. Pan, A. Gupta, *J. Phys. Chem. C* **2015**, *119*, 15506.
[23] J. Y. Kim, G. Magesh, D. H. Youn, J.-W. Jang, J. Kubota, K. Domen, J. S. Lee, *Sci. Rep.* **2013**, *3*, 2681.
[24] V. Jovic, W.-T. Chen, D. Sun-Waterhouse, M. G. Blackford, H. Idriss, G. I. N. Waterhouse, *J. Catal.* **2013**, *305*, 307.
[25] M. Murdoch, G. I. N. Waterhouse, M. A. Nadeem, J. B. Metson, M. A. Keane, R. F. Howe, J. Llorca, H. Idriss, *Nat. Chem.* **2011**, *3*, 489.
[26] Y. Li, H. Yu, C. Zhang, L. Fu, G. Li, Z. Shao, B. Yi, *Int. J. Hydrogen Energy* **2013**, *38*, 13023.
[27] Z. Zhang, L. Zhang, M. N. Hedhili, H. Zhang, P. Wang, *Nano Lett.* **2013**, *13*, 14.
[28] Z. Y. Zhan, J. N. An, H. C. Zhang, R. V. Hansen, L. X. Zheng, *ACS Appl. Mater. Interfaces* **2014**, *6*, 1139.
[29] M. Mishra, D.-M. Chun, *Appl. Catal., A* **2015**, *498*, 126.
[30] F.-W. Chang, H.-Y. Yu, L. S. Roselin, H.-C. Yang, T.-C. Ou, *Appl. Catal., A* **2006**, *302*, 157.
[31] I. A. Rodionov, E. V. Mechtaeva, I. A. Zvereva, *Russ. J. Gen. Chem.* **2014**, *84*, 611.
[32] F. L. Wang, Y. J. Jiang, A. Gautam, Y. R. Li, R. Amal, *ACS Catal.* **2014**, *4*, 1451.
[33] K. Qian, B. C. Sweeny, A. C. Johnston-Peck, W. X. Niu, J. O. Graham, J. S. DuChene, J. J. Qiu, Y. C. Wang, M. H. Engelhard, D. Su, E. A. Stach, W. D. Wei, *J. Am. Chem. Soc.* **2014**, *136*, 9842.
[34] X. Zhang, Y. Liu, S.-T. Lee, S. Yang, Z. Kang, *Energy Environ. Sci.* **2014**, *7*, 1409.
[35] H. G. Baldovi, F. Albarracin, P. Atienzar, B. Ferrer, M. Alvaro, H. Garcia, *ChemPhysChem* **2015**, *16*, 335.
[36] K. E. deKrafft, C. Wang, W. Lin, *Adv. Mater.* **2012**, *24*, 2014.
[37] Z. J. Lin, X. H. Wang, J. Liu, Z. Y. Tian, L. C. Dai, B. B. He, C. Han, Y. G. Wu, Z. G. Zeng, Z. Y. Hu, *Nanoscale* **2015**, *7*, 4114.
[38] A. Petala, E. Ioannidou, A. Georgaka, K. Bourikas, D. I. Kondarides, *Appl. Catal., B* **2015**, *178*, 201.
[39] S. J. A. Moniz, S. A. Shevlin, X. An, Z.-X. Guo, J. Tang, *Chem. Eur. J.* **2014**, *20*, 15571.
[40] X. D. Wang, G. I. N. Waterhouse, D. R. G. Mitchell, K. Prince, R. A. Caruso, *ChemCatChem* **2011**, *3*, 1763.
[41] Y. Xia, L. Yin, *Phys. Chem. Chem. Phys.* **2013**, *15*, 18627.

[42] D. Barreca, G. Carraro, M. E. A. Warwick, K. Kaunisto, A. Gasparotto, V. Gombac, C. Sada, S. Turner, G. Van Tendeloo, C. Maccato, P. Fornasiero, *CrystEngComm* **2015**, *17*, 6219.
[43] S. Zhu, F. Yao, C. Yin, Y. Li, W. Peng, J. Ma, D. Zhang, *Microporous Mesoporous Mater.* **2014**, *190*, 10.
[44] T. Zhu, W. Li Ong, L. Zhu, G. Wei Ho, *Sci. Rep.* **2015**, *5*, 10601.
[45] O. Akhavan, *Appl. Surf. Sci.* **2010**, *257*, 1724.
[46] D. Barreca, G. Carraro, V. Gombac, A. Gasparotto, C. Maccato, P. Fornasiero, E. Tondello, *Adv. Funct. Mater.* **2011**, *21*, 2611.
[47] D. Barreca, G. Carraro, A. Gasparotto, C. Maccato, C. Sada, A. P. Singh, S. Mathur, A. Mettenbörger, E. Bontempi, L. E. Depero, *Int. J. Hydrogen Energy* **2013**, *38*, 14189.
[48] D. Monllor-Satoca, M. Bartsch, C. Fabrega, A. Genc, S. Reinhard, T. Andreu, J. Arbiol, M. Niederberger, J. R. Morante, *Energy Environ. Sci.* **2015**, *8*, 3242.
[49] L. Peng, T. Xie, Y. Lu, H. Fan, D. Wang, *Phys. Chem. Chem. Phys.* **2010**, *12*, 8033.
[50] G. Carraro, A. Gasparotto, C. Maccato, V. Gombac, F. Rossi, T. Montini, D. Peeters, E. Bontempi, C. Sada, D. Barreca, P. Fornasiero, *RSC Adv.* **2014**, *4*, 32174.
[51] D. Barreca, G. Carraro, A. Gasparotto, C. Maccato, M. E. A. Warwick, K. Kaunisto, C. Sada, S. Turner, Y. Gönüllü, T.-P. Ruoko, L. Borgese, E. Bontempi, G. Van Tendeloo, H. Lemmetyinen, S. Mathur, *Adv. Mater. Interfaces* **2015**, *2*, 1500313.
[52] D. Barreca, G. Carraro, A. Gasparotto, C. Maccato, F. Rossi, G. Salviati, M. Tallarida, C. Das, F. Fresno, D. Korte, U. Lavrencič Štangar, M. Franko, D. Schmeisser, *ACS Appl. Mater. Interfaces* **2013**, *5*, 7130.
[53] C. X. Kronawitter, J. R. Bakke, D. A. Wheeler, W.-C. Wang, C. Chang, B. R. Antoun, J. Z. Zhang, J. Guo, S. F. Bent, S. S. Mao, L. Vayssieres, *Nano Lett.* **2011**, *11*, 3855.
[54] X. Li, P. S. Bassi, P. P. Boix, Y. Fang, L. H. Wong, *ACS Appl. Mater. Interfaces* **2015**, *7*, 16960.
[55] S. Linic, P. Christopher, D. B. Ingram, *Nat. Mater.* **2011**, *10*, 911.
[56] Q. Simon, D. Barreca, A. Gasparotto, C. Maccato, T. Montini, V. Gombac, P. Fornasiero, O. I. Lebedev, S. Turner, G. Van Tendeloo, *J. Mater. Chem.* **2012**, *22*, 11739.
[57] Y. Liu, Z. Wei, T. Xing, M. Lu, X. Li, *J. Ind. Eng. Chem.* **2015**, *23*, 321.
[58] M. A. Mahadik, S. S. Shinde, H. M. Pathan, K. Y. Rajpure, C. H. Bhosale, *J. Photochem. Photobiol., B* **2014**, *141*, 315.
[59] Y.-F. Yang, P. Sangeetha, Y.-W. Chen, *Ind. Eng. Chem. Res.* **2009**, *48*, 10402.
[60] R. Ahmad, N. Griffete, A. Lamouri, N. Felidj, M. M. Chehimi, C. Mangeney, *Chem. Mater.* **2015**, *27*, 5464.
[61] Pattern No. 33-0664, JCPDS (**2000**).
[62] D. Eisenberg, H. S. Ahn, A. J. Bard, *J. Am. Chem. Soc.* **2014**, *136*, 14011.
[63] J. F. Moulder, W. F. Stickle, P. E. Sobol, K. D. Bomben, *Handbook of X-ray Photoelectron Spectroscopy*, Perkin Elmer Corporation, Eden Prairie, MN, USA **1992**.
[64] G. Carraro, A. Gasparotto, C. Maccato, E. Bontempi, F. Bilo, D. Peeters, C. Sada, D. Barreca, *CrystEngComm* **2014**, *16*, 8710.
[65] M. C. Toroker, D. K. Kanan, N. Alidoust, L. Y. Isseroff, P. Liao, E. A. Carter, *Phys. Chem. Chem. Phys.* **2011**, *13*, 16644.
[66] X. Chen, L. Liu, P. Y. Yu, S. S. Mao, *Science* **2011**, *331*, 746.
[67] G. Carraro, D. Barreca, D. Bekermann, T. Montini, A. Gasparotto, V. Gombac, C. Maccato, P. Fornasiero, *J. Nanosci. Nanotechnol.* **2013**, *13*, 4962.
[68] J. Li, N. Wu, *Catal. Sci. Technol.* **2015**, *5*, 1360.
[69] Y. J. Hwang, C. Hahn, B. Liu, P. Yang, *ACS Nano* **2012**, *6*, 5060.
[70] G. Carraro, A. Gasparotto, C. Maccato, E. Bontempi, D. Barreca, *Chem. Vap. Deposition* **2015**, *21*, 294.
[71] E. Toniato, *Master Thesis*, Padova University, Italy, **2016**.
[72] D. Briggs, M. P. Seah, *Practical Surface Analysis: Auger and X-ray Photoelectron Spectroscopy*, 2nd ed., John Wiley & Sons, New York **1990**.